Mechanics & Industry **24**, 18 (2023)

https://doi.org/10.1051/meca/2023005

Mechanics & Industry

Available online at:
www.mechanics-industry.org

Regular Article

Open Access

Research and control of a new dual-modulation magnetic gear compound motor for electric vehicles based on a mathematical model and FEA co-simulation

Jun-Gang Wang[1,*], Bin Zhang[2], and Li-Qun Qian[1,2]

[1] School of Mechatronics and Vehicle Engineering, East China Jiaotong University, Nanchang 330000, China
[2] Key Laboratory of Conveyance and Equipment, Ministry of Education, East China Jiaotong University, Nanchang 330013, Jiangxi, China

Received: 19 December 2021 / Accepted: 27 January 2023

Abstract. According to the development of the electric vehicle motor drives, a magnetic gear compound motor with small size, lightweight, non-contact, and high-power has a good development prospect in the new energy electric vehicle industry. A new dual-modulation magnetic gear compound motor (DMFMCM) with high torque, low torque ripple, and high mechanical strength is proposed in the paper. The topology and driving principle of DMFMCM are analyzed in this paper, and the finite elements analysis (FEA) is used to compare and analyze the DMFMCM and the conventional magnetic gear compound motor (CMGCM). Furthermore, the mathematical model of DMFMCM is established to achieve the decoupling of the three-phase voltage or current, and the mathematical model and FEA co-simulation is established to ensure the accuracy of the mathematical model. Finally, according to the principle of SVPWM controlled by $i_d = 0$, the paper simulates a PI-adjusted three-phase DMFMCM control system model. The result shows that the DMFMCM controlled by SVPWM has high stability, strong anti-interference ability and good speed regulation performance, thus meeting the development of electric vehicles.

Keywords: Magnetic gear compound motor / dual-modulation / simulation / SVPWM

1 Introduction

In order to respond to the sustainable social development trend, electric vehicles have gradually replaced traditional fuel vehicles in the automotive industry. Electric vehicles convert electrical energy into mechanical energy by driving motors, which are environmentally friendly, stable, efficient and more convenient to operate than traditional fuel vehicles [1–3]. In order to respond to the trend of sustainable social development, the drive motor should have the characteristics such as low speed, high torque, high stability, and good safety and comfort [4–5].

The power system of electric vehicles is generally composed of a drive motor and a gear transmission system. The driving motors of electric vehicles mainly include DC motors, induction motors, switched reluctance motors, and permanent magnet motors [6]. The principle of the DC motor is simple, and the torque control is simple. However, its volume is usually large, the energy density and power density are low, and the commutation device has a life limit. Therefore, there are certain restrictions on the use of electric vehicles [7]. The induction motor has a simple structure and high reliability. However, with its electrically exciting system, the copper and eddy current losses can lead to lower efficiency and higher control costs. [8]. Switched reluctance motors have the characteristics of a simple rotor structure, high mechanical strength and reliability. However, the switched reluctance motor has high torque fluctuations at low speeds, which will seriously affect the comfort of electric vehicles during starting, braking and low-speed driving [9]. In contrast, permanent magnet synchronous motors use permanent magnets instead of excitation winding. Permanent magnet synchronous motors reduce the copper and eddy current losses caused by the field current, so the motor efficiency is higher [10]. The permanent magnet motor is combined with the magnetic gear to form a compound motor with integrated drive and transmission. The transmission system of the magnetic gear compound motor has a transmission ratio, which can realize variable speed transmission. In addition, the magnetic gear compound motor has the advantages of

* e-mail: mewjg@ecjtu.edu.cn

small size, lightweight, low friction loss, convenient control, and high efficiency, which can meet the driving performance requirements of electric vehicles.

The magnetic gear compound motor, a new direct-drive motor with low speed and high torque characteristics, was proposed by Professor K.T. Chau of the University of Hong Kong in 2009. This compound motor makes the magnetic gear and the permanent magnet motor share a rotor to form a compound structure, which improves the efficiency and power density of the device [11]. However, the compound motor has three air gaps, which are not conducive to control, and the rotor surface attaches to three layers of permanent magnets, which will fall off when the motor rotates at high speed. In 2014, Fan Ying from Southeast University in China proposed a unipolar permanent magnet arrangement magnetic gear compound motor with a self-deceleration function [12]. This structure adds a modulation ring between the rotor and the stator to achieve variable-speed transmission. In addition, the two-layer air gap reduces the magnetic leakage phenomenon, which improves motor torque. In 2017, K. Atallah from the University of Sheffield in the UK proposed a pseudo-direct drive magnetic gear compound motor [13]. The motor adopts an outer stator structure and has permanent magnets attached to the stator teeth, so there is one less air gap than the traditional magnetic gear compound motor. According to the analysis and experiment, the feasibility of the variable winding structure is verified, and the magnetic leakage phenomenon is reduced. In the same year, S.X. Niu from the Hong Kong Polytechnic University proposed a double-pole magnetic gear compound motor [14]. The outer rotor and the modulation ring have equal permanent magnets, so the two layers of permanent magnets are combined with iron sheets to form a modulation ring with modulation. Compared with the single-pole magnetic gear compound motor, this structure has a higher torque density and is more suitable for direct-drive systems with low speed and high torque. In addition, Hang Zhao from the City University of Hong Kong proposed a dual-modulator magnetic gear reduction motor in 2020 [15]. The motor structure adds a modulator outside the spoke-type permanent magnet motor, which makes it have a magnetic flux focusing effect and increases the flux density on the air gap to increase the torque. In summary, it can be found that the magnetic gear compound motor will strive to simplify the mechanical structure of the compound motor, reduce the number of air gap layers, and increase the torque density and reduce torque ripple.

In order to improve the performance of the drive motor, it is not only necessary to optimize the electromagnetic structure of the motor but also to realize the control algorithm. The controller is an important part of the electric vehicle, and the control algorithm is its core elements. In recent years, motor control technology is keeping maturing, providing reliable technical support for magnetic gear compound motors. The magnetic gear compound motor is a multi-variable and strongly coupled control object. Therefore, decoupling its control parameters is the most effective way to improve the accuracy of the control algorithm, and vector control and direct torque control are the most common decoupling control strategies [16–18]. Although direct torque control has a low degree of model dependence, it has a longer control cycle and a smaller motor inductance. During startup and load changes, the torque ripple of the motor is relatively large. In addition, it is difficult to accurately observe the flux linkage and torque when the motor is at low speeds, and it is also hard to achieve high-performance control of the motor torque and flux linkage [19]. Vector control is also called field-oriented control, and the control effect is based on the accurate mathematical model of the controlled object. By decoupling the stator current, the vector control decomposes the current into electromagnetic torque current and excitation current, and then the two currents are independently controlled. The vector control system can ensure the torque of the actual load object, produce stable electromagnetic torque, and have a wide range of speed regulation. During the starting and braking, the armature current of the motor generates electromagnetic torque, which can make full of the overload capacity of the motor and improve the starting and braking performance [20,21]. Therefore, although the vector control relies on the accuracy of the mathematical model, the drive motor using the control method has better system stability and faster response speed. Commonly used vector control methods include $i_d = 0$ control, $\cos\varphi = 1$ control, maximum torque/current ratio control, field weakening control, and maximum efficiency control. Among them, the effect of $i_d = 0$ control is comparable to that of DC motors, especially in the low-speed control range, the control effect is more prominent [22–24]. Therefore, the $i_d = 0$ control is the most used in the vector control method.

According to the development trend of the magnetic gear compound motor, a new dual-modulation magnetic gear compound motor (DMFMCM) applied to electric vehicles is proposed. The DMFMC is to improve the torque density of the magnetic gear compound motor, suppress the torque ripple, enhance the mechanical structure, and improve the reliability and stability of the motor during operation. The magnetic gear compound motor proposed in this paper combines the modulation pieces with the stator teeth to reduce an air gap, which is convenient for the assembly of the motor. Furthermore, it can realize the secondary speed modulation and increase the gear ratio. Then, the space vector pulse width modulation (SVPWM) method with $i_d = 0$ is used to control the speed of the DMFMCM so that the conversion of the motor speed is more stable. Based on the research of motor performance, this paper establishes mathematical model and finite elements analysis (FEA) co-simulation of DMFMCM to verify the accuracy of the mathematical model. In addition, a Simulink simulation model based on the mathematical model was established to verify the motor parameters during motor control. After ensuring the accuracy of the mathematical model, the SVPWM with $i_d = 0$ is adopted for DMFMCM, which makes the motor have better performance to meet the needs of the electric vehicles, and build the SVPWM control module simulation model.

2 Analysis and research of DMFMCM

The magnetic gear compound motor is a structure that can realize low-speed and high-torque transmission, which has a good application prospect in the field of new energy such as wind power generation and electric vehicles. Figure 1 shows the topology of DMFMCM. The outer rotor of DMFMCM adopts a salient pole structure. When the convex pole coefficient $\delta_e = 0$, it is a uniform permanent magnet; when the convex pole coefficient $\delta_e > 0$, the permanent magnet is convex; when $\delta_e < 0$, the permanent magnet is concave. The DMFMCM uses a convex pole factor of 0.5, i.e. the ratio of the protrusion of the permanent magnet to the width of the air gap is 0.5. The permanent magnets of the inner rotor have a tangential magnetized spoke-type structure with pole shoes embedded between the permanent magnets, which can form a flux-magnetic structure. In addition, the magnetic gear compound motor combines the modulated pieces and stator teethes, which makes the stator have the effect of magnetic field modulation. Therefore, the magneto-gear compound motor reduces an air gap and achieves a twice modulating effect of the stator teeth and the modulation ring. Furthermore, this salient pole of the permanent magnets and the flux-magnetic structure effectively enhance the torque density, increase the utilization of the permanent magnets and reduce the magnetic leakage. Therefore, the DMFMCM can effectively increase torque and suppress torque ripple [25,26].

The parameters of DMFMCM are shown in Table 1.

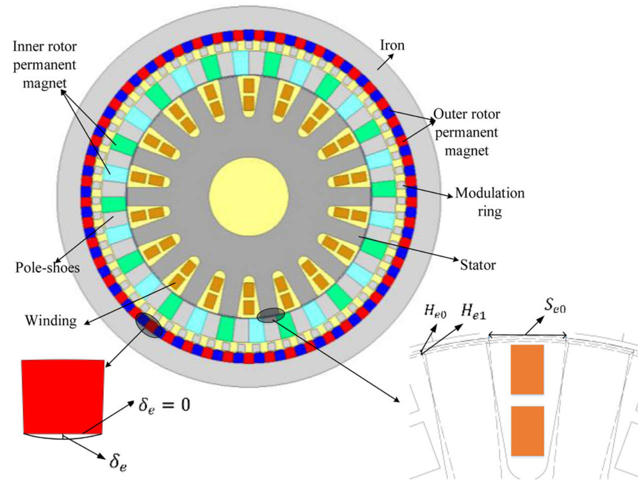

Fig. 1. Topology of DMFMCM.

Table 1. Parameters of DMFMCM.

Parameter	Values
Axial length of DMFMCM	65 mm
Number of stator slots	18
Pole pairs number of armature winding	4
Pole pairs number of inner rotor permanent magnets	14
Pole pairs number of outer rotor permanent magnets	49
The number of modulation ring poles	63
Gear ratio	2:7
Rotating speed	214 r/min
Material of stator and rotor core	DW360-50
Inner diameter of the inner rotor	154 mm
Outer diameter of the outer rotor	184 mm
Thickness of the modulation pieces	5 mm
Radial length of permanent magnet	30 mm
Width of permanent magnet	15 mm
Maximum thickness of the air gap	1 mm
Remanence	1.21T
Relative permeability	1.07
Radius of air gap	153 mm
Permanent magnet material	NdFeB
Width of air gap	1 mm
Number of air gaps	3

2.1 Topology of DMFMCM drive system

The driving system of DMFMCM studied in this paper is a three-phase 18-slot/28-pole field modulation permanent magnet motor (FMPMM). The three-phase alternating current is applied to the winding coil of DMFMCM, which makes the energized winding generate a rotating magnetic field to couple with the FMPMM motor rotor and generate torque. The torque generated by the rotor of FMPMM is coupled with the outer permanent magnet rotor through the outer modulation ring so that the outer rotor generates torque to work.

The topological structure of the drive system FMPMM is shown in Figure 2. The rotor of FMPMM adopts a tangentially magnetized spoke structure, and the pole shoes are embedded between the permanent magnets to increase the torque. The stator adopts a slotted structure, and the stator teeth and the modulation pieces are combined to form a permanent magnet motor with field modulation. Due to the combination of the modulated block with the stator teeth, the two air gaps that would have been required with the addition of the modulating ring become one air gap. Therefore, the motor reduces the air gap and suppresses the magnetic leakage.

2.2 The principle of torque generated by DMFMCM

2.2.1 The working principle of the magnetic gear

With the introduction of the modulation ring, the air gap space in the magnetic gear section is divided into two layers of the air gap. Due to the magnetic permeability of the modulation pieces is much greater than the air permeability, the magnetic path in the radial direction of the air gap is uneven, resulting in a change in the magnetic flux density in the air gap. The magnetic field modulation of modulation ring can be expressed by the air gap permeability function

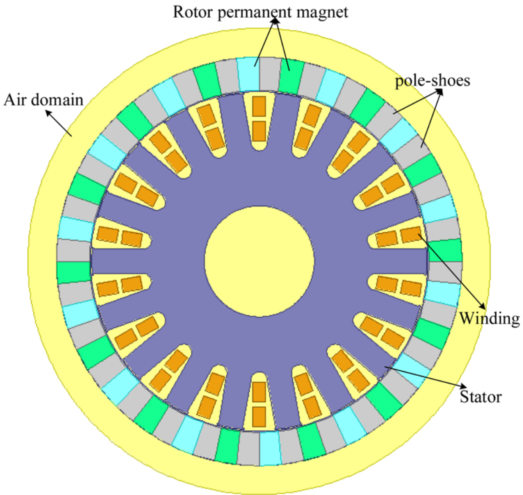

Fig. 2. Topology of FMPMM.

$$\lambda_{rp}(r)=\lambda_{rp}^{0}(r)+\sum_{j=1}^{+\infty}\lambda_{rp}^{j}(r)\cos[jn_p(\theta-\omega_p t)+jn_p\varphi_{rj}] \quad (1)$$

$$\lambda_{\theta p}(r)=\lambda_{\theta p}^{0}(r)+\sum_{j=1}^{+\infty}\lambda_{\theta p}^{j}(r)\sin[jn_p(\theta-\omega_p t)+jn_p\varphi_{\theta p}] \quad (2)$$

where j represents the harmonics number, ω_p represents the modulation ring speed, $\varphi_{\theta p}$ and φ_{rp} respectively represent the initial radial and tangential angles of modulation ring, $\lambda_{\theta p}^{0}$, λ_{rp}^{0}, $\lambda_{\theta p}^{j}$ and λ_{rp}^{j} represent Fourier coefficients.

The permanent magnets of the inner rotor are embedded in pole-shoes and distributed along the circumference. Therefore, the pole-shoes and the modulation ring have a similar modulation effect. The specific expression is as follows

$$\lambda_{rs}(r)=\lambda_{rs}^{0}(r)+\sum_{k=1}^{+\infty}\lambda_{rs}^{k}(r)\cos[kn_s(\theta-\omega_s)+kn_s\varphi_{rs}] \quad (3)$$

$$\lambda_{\theta s}(r)=\lambda_{\theta s}^{0}(r)+\sum_{k=1}^{+\infty}\lambda_{\theta s}^{k}(r)\sin[kn_s(\theta-\omega_s)+kn_s\varphi_{\theta s}] \quad (4)$$

where k represents the harmonics number, n_s represents the pole-shoes number, ω_s is the pole-shoes speed, $\varphi_{\theta s}$ and φ_{rs} respectively represent the initial radial and tangential angles of the pole-shoes, $\lambda_{\theta s}^{0}$, λ_{rs}^{0}, $\lambda_{\theta s}^{k}$ and λ_{rs}^{k} represent Fourier coefficients.

According to the modulating effect of the modulating commutation and pole shoe, The radial flux density distribution produced by the permanent magnet rotor is expressed as follows.

$$\begin{aligned}B_r(r)=&\sum_{j=0,\pm1,\pm2}^{+\infty}\sum_{k=0,\pm1,\pm2}^{\pm\infty}\sum_{a=1,3,5}^{\pm\infty}b_r^{j,k,a}(r)\\&\times\cos\Big[\big(pa+jn_p+kn_s\big)\\&\times\left(\theta-\frac{pa\omega_r+jn_p\omega_p+kn_s\omega_s}{pa+jn_p+kn_s}t\right)\\&+pa\varphi_r+jn_p\varphi_{rp}+kn_s\varphi_{rs}\Big]\end{aligned} \quad (5)$$

where $b_r^{j,k,a}$ represents Fourier coefficients.

The tangential magnetic flux distribution produced by any rotor is calculated as follows.

$$\begin{aligned}B_\theta(r)=&\sum_{j=0,\pm1,\pm2}^{+\infty}\sum_{k=0,\pm1,\pm2}^{\pm\infty}\sum_{a=1,3,5}^{\pm\infty}b_r^{j,k,a}(r)\\&\times\sin\Big[\big(pa+jn_p+kn_s\big)\\&\times\left(\theta-\frac{pa\omega_r+jn_p\omega_p+kn_s\omega_s}{pa+jn_p+kn_s}t\right)\\&+pa\varphi_\theta+jn_p\varphi_{\theta p}+kn_s\varphi_{\theta s}\Big]\end{aligned} \quad (6)$$

where $b_\theta^{j,k,a}$ represents Fourier coefficients.

The spatial harmonic pole logarithm contained in the air gap magnetic field of the magnetic gear proposed in this paper is expressed as follows.

$$p_{j,k,m}=|pa+jn_p+kn_s|$$

where $a=1, 3, 5, \ldots, \infty$, $j=0, \pm1, \pm2, \pm3, \ldots, \pm\infty$ $k=0, \pm1, \pm2, \pm3, \ldots, \pm\infty$. (7)

According to the operation principle of CMG in [8], the modulated pole-pieces number and PM pole-pairs should be satisfied as (8),

$$n_p=p_i+p_o. \quad (8)$$

From the above equation, the pole-shoes and outer rotor will generate p_i+n_s pole-pairs harmonics. Similarly, the modulated ring and outer rotor will produce p_o+n_p pole-pairs harmonics

$$p_i+n_s=p_o+n_p. \quad (9)$$

The Fourier expansion of the magnetic induction intensity at a certain position is

$$\begin{cases}B_\theta=\sum\limits_k B_{\theta k}\cos(k\alpha-\alpha_{\theta k})\\ B_r=\sum\limits_k B_{rk}\cos(k\alpha-\alpha_{rk})\end{cases} \quad (10)$$

where B_r represents the radial magnetic field component, B_θ represents the tangential magnetic field component. B_{rk} and $B_{\theta k}$ respectively represent the kth Fourier coefficients of the radial and tangential component. α_{rk} and $\alpha_{\theta k}$ are the kth phase angles at that position. The harmonic torque of the k_{th} order is obtained according to Maxwell tensor method as

$$T_k = \frac{\pi r^2 l_{ef}}{\mu_o} B_{rk} B_{\theta k} \cos(\alpha_{rk} - \alpha_{tk}) \tag{11}$$

where r represents the air-gap radius, μ_0 represents the vacuum permeability, and l_{ef} represents the axis length.

2.2.2 The working principle of FMPMM

The electromechanical energy conversion of the magnetic gear compound motor is carried out by the magnetic field generated by the rotor and the armature winding. Based on the equivalent magnetic circuit method, the magnetic circuit can be analogous to an electric circuit to simplify the calculation and analysis process of the motor. It can be regarded as a loop composed of permanent magnets, magneto-motive force source and air gap. In order to simplify the electromagnetic torque derivation process of FMPMM, it is assumed that the magnetic field changes only in the cross-section, and the local magnetic saturation and flux leakage of the iron core are ignored. In the process of analyzing the change of air gap permeability, the equivalent air gap length $\delta_g{}'$ is as follows.

$$\delta_{g'} = k_c \delta_g \tag{12}$$

where δ_g is the length of the air gap, k_c is the Carter coefficient.

Due to the permanent magnet rotor using high-performance NdFeB, the demagnetization curve changes linearly, and the characteristics of the second quadrant can be approximated as a straight line [27]. Therefore, the permanent magnet can be equivalent to a magnetomotive force source with constant outer reluctance. The magnetic circuit analysis model of FMPMM and various parameters are shown in Figure 3a. Where θ_m is the thickness of the permanent magnet, r_g is the air gap radius, l_m is the radial length of the permanent magnet, and θ_p is the thickness of the rotor core. According to the known parameters, the permanent magnet magnetomotive force F_m can be calculated as follows.

$$F_m = \frac{B_r}{\mu_0 \mu_{rm}} \theta_m r_g \tag{13}$$

where B_r is the remanence, μ_0 is the vacuum permeability, and μ_{rm} is the relative permeability. The outer magnetic resistance R_m of the permanent magnet is calculated as (3).

$$R_m = \frac{\theta_m r_g}{\mu_0 \mu_m l_m L_a} \tag{14}$$

where L_a is the axial length of FMPMM, and the equivalent air gap magnetoresistance R_g can be expressed as (14).

$$R_g = \frac{2\delta_{g'}}{\mu_0 \theta_p r_g L_a} \tag{15}$$

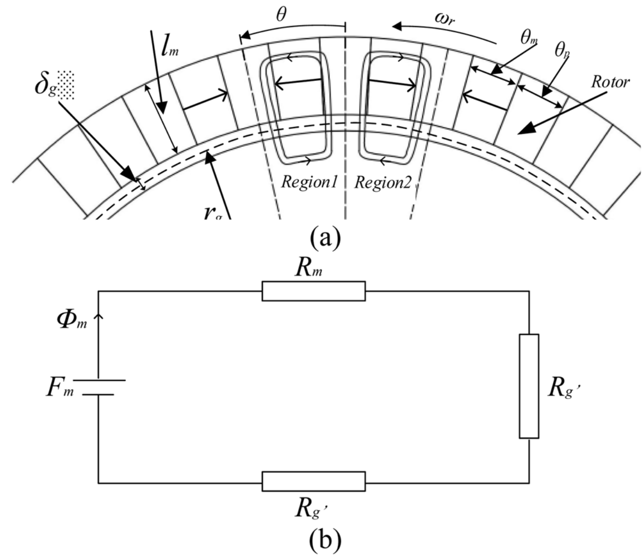

Fig. 3. (a) Magnetic circuit analysis model of FMPMM; (b) equivalent magnetic circuit of FMPMM.

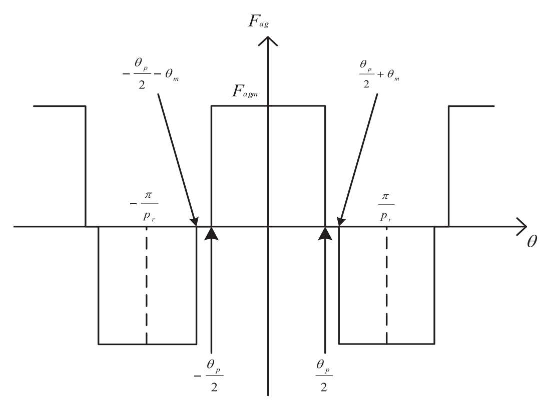

Fig. 4. Equivalent air gap magnetomotive force waveform of FMPMM.

According to the magnetic flux low, it can be found that the magnetic flux of the rotor is calculated as follows.

$$\Phi_m = \frac{F_m}{R_m + 2R_{g'}} = \frac{B_r \theta_m r_g^2 l_m L_a}{\theta_m \theta_p r_g^2 + 4\delta_g \mu_m l_m}. \tag{16}$$

The amplitude of air gap magnetomotive force can be expressed as follows.

$$F_m = \Phi_m R_{g'} = \frac{2B_r \theta_m r_g l_m \delta_{g'}}{\mu_0 \theta_m \theta_p r_g^2 + 4\mu_0 \mu_{rm} \delta_g l_m}. \tag{17}$$

Based on the calculation and analysis, the air gap magnetomotive force waveform of FMPMM can be equivalent to a square wave is shown in Figure 4. Considering the rotation of the rotor, and according to

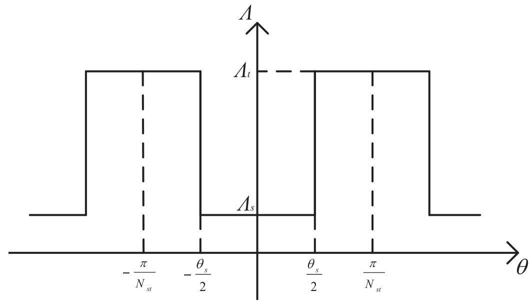

Fig. 5. The simplified air gap permeance waveform.

the Fourier transform, the calculation formula for the change of the air gap magnetomotive force F_{ag} with the circumferential position θ can be obtained as follows.

$$F(\theta,t)=\sum_{j=1,3,5}^{+\infty}F_j\cos[jp_r(\theta-\omega_r t)] \tag{18}$$

where p_r is the pole pairs number of the rotor, and the jth component amplitude F_{agj} is calculated as (18).

$$\begin{aligned}F_j&=\frac{p_r}{\pi}\int_{-\frac{\pi}{p_r}}^{\frac{\pi}{p_r}}F(\theta)\cos(jp_r\theta)d\theta\\&=\frac{4F_m}{j\pi}\sin\left(\frac{j\pi}{2}\right)\cos\left(\frac{jp_r\theta_m}{2}\right)\end{aligned}. \tag{19}$$

The above is a simplified analysis of the change in permeability caused by the change in the stator tooth slot with the aid of an equivalent air gap. In the following, the effect of the stator tooth slot change on the air gap permeability is considered, and the air gap permeability is calculated. Figure 5 shows the simplified air gap permeability waveform considering the stator tooth slot alternation. The permeability λ_t and λ_s at the corresponding air gap of the stator tooth slot can be expressed as follows.

$$\lambda_t=\frac{\mu_0\theta_t r_g L_a}{\delta_g} \tag{20}$$

$$\lambda_s=\frac{4\mu_0 L_a}{\pi}\ln\left(1+\frac{\pi\theta_s r_g}{4\delta_g}\right), \tag{21}$$

where θ_t is the width of the stator teeth, and θ_s represents the width of the slots.

According to the permeance waveform and using Fourier transform, it can be seen that the calculation for the change of the air gap permeance with the position angle θ is as follows.

$$\lambda(\theta)=\lambda_0+\sum_{i=1,2,3}^{+\infty}\lambda_i\cos(iN_{st}\theta) \tag{22}$$

where λ_0 is the DC component, N_{st} is the number of stator teeth, and the expression is as (22).

$$\lambda_0=\frac{N_{st}}{2\pi}(\lambda_t\theta_t+\lambda_s\theta_s) \tag{23}$$

The harmonic component λ_i is calculated as follows.

$$\begin{aligned}\lambda_i&=\frac{N_{st}}{\pi}\int_{-\frac{\pi}{N_{st}}}^{\frac{\pi}{N_{st}}}\lambda(\theta)\cos(iN_{st}\theta)d\theta\\&=\frac{2(\lambda_s-\lambda_t)}{i\pi}\sin\left(\frac{iN_{st}\theta_s}{2}\right)\end{aligned}. \tag{24}$$

In summary, it can be found that the air gap flux density of the DMFMCM is calculated as follows

$$\begin{aligned}B(\theta,t)&=\lambda_0F_1\cos[p_r(\theta-\omega_r t)]+\lambda_1F_1\cos(N_{st}\theta)\\&\times\cos[p_r(\theta-\omega_r t)]+B_h\\&=\lambda_0F_1\cos[p_r(\theta-\omega_r t)]+\frac{\lambda_1F_1}{2}\\&\times\cos\left[(N_{st}-p_r)\left(\theta+\frac{p}{N_{st}-p_r}\omega_r t\right)\right]\\&+\frac{\lambda_1F_1}{2}\cos\left[(N_{st}+p_r)\left(\theta-\frac{p}{N_{st}-p_r}\omega_r t\right)\right]+B_h\end{aligned} \tag{25}$$

where B_h is the high-order magnetic density harmonic component, which occupies a small proportion and it can be ignored. The formula shows that the fundamental component with the same number of rotor pole pairs, there are also N_{st-pr} and N_{st+pr} pairs of harmonic magnetic fields. In a three-phase permanent magnet motor, the formula of the phase flux linkage is as follows.

$$\psi_p(t)=k_dN_pL_ar_g\int_0^{\sigma\theta_\tau}B(\theta,t)d\theta \tag{26}$$

where k_d is the fundamental distribution coefficient of the winding, N_p is the number of turns in series, and σ is the coil span. Furthermore, the stator slot pitch θ_τ can be expressed as (26).

$$\theta_\tau=\theta_t+\theta_s=\frac{2\pi}{N_{st}} \tag{27}$$

The expression of the phase flux linkage of the DMFMCM can be obtained as shown in (27) by combining (24) and (25).

$$\begin{aligned}\psi_{ph}(t)&=k_dN_pL_ar_g\times\left\{\frac{2\lambda_0F_1}{(2q-1)}\sin\left[\left(1-\frac{1}{2q}\right)\sigma\pi\right]\right.\\&\times\cos\left[\left(1-\frac{1}{2q}\right)\sigma\pi-(2q-1)p_s\omega_r t\right]+\frac{\lambda_1F_1}{p_s}\\&\times\sin\left(\frac{1}{2q}\sigma\pi\right)\cos\left[\frac{1}{2q}\sigma\pi+(2q-1)p_s\omega_r t\right]\end{aligned} \tag{28}$$

where q is the number of stator slots per pole.

The induced electromotive force of FMPMM is as follows.

$$E_{ph}(t) = k_d N_p L_a r_g \omega_r \times \left\{ \begin{array}{l} 2\lambda_0 F_1 \sin\left(G_r \frac{\sigma\pi}{2q}\right) \times \sin\left(G_r p_s \omega_r t - G_r \frac{\sigma\pi}{2q}\right) \\ +G_r \lambda_1 F_1 \sin\left(\frac{\sigma\pi}{2q}\right) \times \sin\left(G_r p_s \omega_r t + \frac{\sigma\pi}{2q}\right) \end{array} \right\}. \tag{29}$$

The FMPMM is an 18-slot/28-pole permanent magnet synchronous machine. The winding pole pair p_s is 4, the gear ratio G_r between the inner rotor and the winding is 3.5, the number of stator slots per pole is 2.25, and the coil span σ is 2. Substituting the parameters into equation (18) above gives the phase induction potential amplitude of the FMPMM as follows.

$$E_{ph} = k_d N_p L_a r_g \omega_r (1.97\lambda_0 F_1 - 3.45\lambda_1 F_1). \tag{30}$$

In order to analyze the electromagnetic torque of FMPMM, using the brushless AC control method with $i_d = 0$, the electromagnetic torque T_e of the permanent magnet motor is expressed as follows.

$$T_e = \frac{m I_m}{2} k_d N_p L_a r_g (1.97\lambda_0 F_1 - 3.45\lambda_1 F_1). \tag{31}$$

In order to verify the accuracy of the above theory, an FEA analysis was performed on the FMPMM. The 2D model of FMPMM can be constructed using AutoCAD software and then imported into Maxwell FEA simulation software, or it can be created directly in Maxwell software. By feeding three-phase currents into the windings and simulating the model, the FMPMM air-gap flux density distribution and harmonic analysis are obtained in Figure 6. It can be found from the figure that the stator teeth will cause the air-gap flux density to generate some spatial harmonics. In addition to the fundamental components with the same number of rotor pole pairs, N_{st-pr} and N_{st+pr} pairs harmonic component with larger amplitudes are generated. Therefore, it can be seen that the FEA analysis is consistent with the theoretically derived flux density expression (24). According to the equivalent circuit method of FMPMM and FEA, the working principle of the torque generated by the drive system of DMFMCM is determined to drive the entire compound motor to operate.

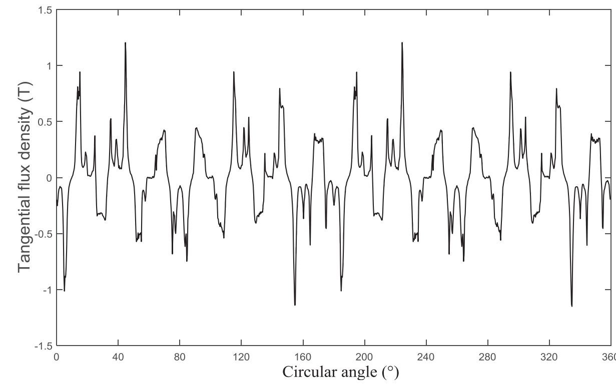

(a)

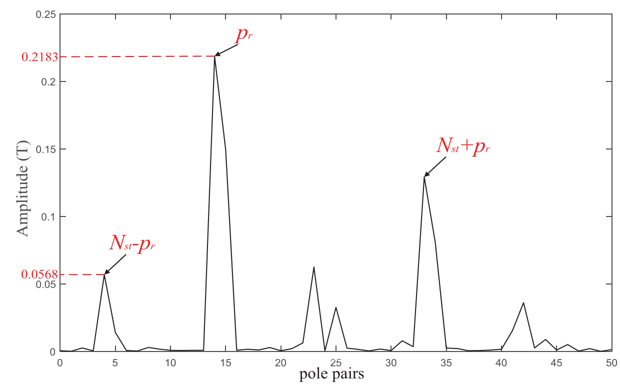

(b)

Fig. 6. (a) Flux density waveform of FMPMM, (b) flux density harmonic of FMPMM.

2.3 Comparison and analysis of DMFMCM and the conventional magnetic gear compound motor (CMGCM)

DMFMCM generates a rotating magnetic field by passing an alternating current, which couples with the permanent magnets on the spoke rotor through the stator teeth and drives the rotor to rotate. Then the rotating magnetic field is coupled with the outer rotor through the modulation ring to make the outer rotor rotate and work. In order to verify the superiority of DMFMCM, an FEA simulation model of the traditional 18-slot magnetic gear compound motor (CMGCM) was established for comparison and analysis with DMFMCM. The FEA simulation results of the outer rotor torque of the two structures are compared to analyze their performance differences.

Based on the principle of quantitative comparison, the number of permanent magnets used to the two motors is the same, and the size of the motor are the same. The FEA is used to obtain the magnetic field distribution of two compound motors as shown in Figure 7.

As shown in Figure 8, the torque of DMFMCM is significantly higher than that of CMGCM, and the torque ripple of DMFMCM is significantly lower than that of CMGCM. According to (31), the torque ripple can be obtained in Table 2. It can be found that the static torque of DMFMCM is 321.02Nm, and it is 1.4 times that of CMGCM. Furthermore, the torque ripple of DMFMCM is 0.19%, which is 29.3% of CMGCM.

$$T_{ripple} = \frac{T_{\max} - T_{\min}}{T_{avg}} \times 100\% \tag{32}$$

where T_{ripple} is the torque ripple, $T_{\max}$ is the maximum torque, $T_{\min}$ is the minimum torque, and T_{avg} is the average electromagnetic torque.

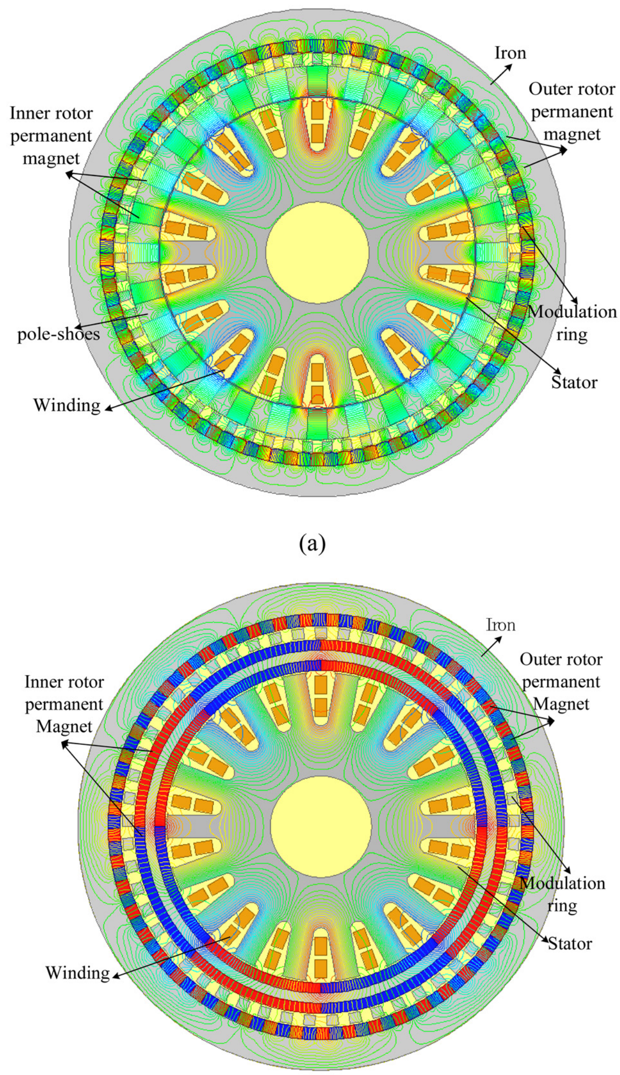

Fig. 7. (a) Magnetic field distribution of DMFMCM, (b) magnetic field distribution of CMGCM.

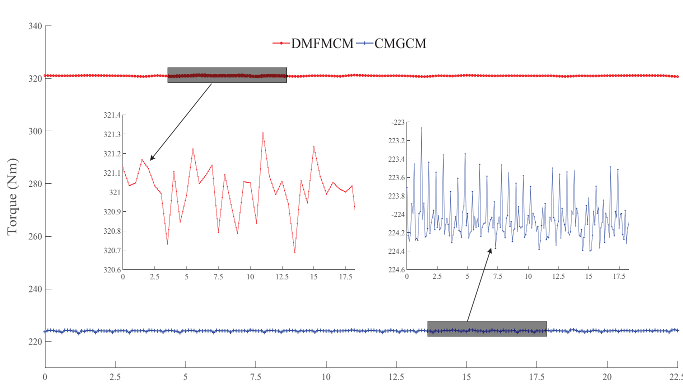

Fig. 8. The torque of the outer rotor calculated by the FEA.

Table 2. Average electromagnetic torque and torque ripple.

Type	T_{avg}	T_{ripple}
DMFMCM	321.02 Nm	0.19%
CMGCM	224.05 Nm	0.65%

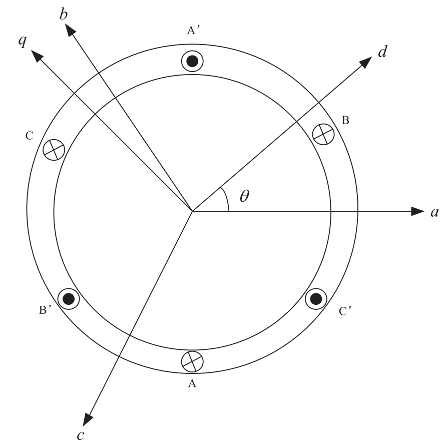

Fig. 9. The *abc* coordinate system and *d*-*q* coordinate system.

3 Mathematical model of DMFMCM

The mathematical model of the drive motor is the basis of the simulation modelling and the analysis and design of the control system. Therefore, according to the electromagnetic characteristics of DMFMCM, a mathematical model under the two-phase rotating coordinate system is established. The FEA method is used to verify the results of the mathematical model to ensure its accuracy. In addition, a simulation model of DMFMCM is built by Simulink components to verify the motor parameters of the control system.

The mathematical model of the three-phase static coordinate system (*abc* coordinate system) based on the stator armature windings of the motor is shown in Figure 9. There are three-phase symmetrical windings A, B, and C on the stator, which differ by 120° in electrical angle. d axis is on the direction of the permanent magnet pole axis of the rotor, and q is advanced by 90° in the counterclockwise direction of the rotor. Take a reference axis, the electrical angle between the d and the reference axis is θ. Based on the analysis method of the mathematical model, the flux linkage equation, voltage equation and torque equation of DMFMCM are established in *abc* coordinate system and the two-phase rotating coordinate system (*d*-*q* coordinate system).

3.1 Mathematical model in *abc* coordinate system

The total flux linkage of each winding of DMFMCM includes permanent magnet flux linkage and armature reaction flux linkage. Therefore, the flux equation expression of

DMFMCM is as follows.

$$\begin{bmatrix}\psi_a\\ \psi_b\\ \psi_c\end{bmatrix}=\begin{bmatrix}L_{aa} & M_{ab} & M_{ac}\\ M_{ba} & L_{bb} & M_{bc}\\ M_{ca} & M_{cb} & L_{cc}\end{bmatrix}\begin{bmatrix}i_a\\ i_b\\ i_c\end{bmatrix}+\begin{bmatrix}\psi_s\cos\theta\\ \psi_s\cos(\theta-120°)\\ \psi_s\cos(\theta+120°)\end{bmatrix} \tag{33}$$

where ψ_a,ψ_b and ψ_c are the total flux linkages of the three-phase windings; i_a, i_b, i_c are the phase currents of the three-phase windings; L_{aa},L_{bb},L_{cc} are the self-inductances of the phase windings; M_{ab},M_{ac},M_{ba},M_{bc},M_{ca},M_{cb} are the mutual inductances of the phase windings; ψ_s is the amplitude of the phase permanent magnet flux of the winding turn chain; θ is the electrical angle of the rotor.

When the brushless AC control mode with $i_d=0$ is adopted, the three-phase current of the motor is expressed as follows.

$$\begin{cases} i_a=I_m\sin(\theta)\\ i_b=I_m\sin(\theta-120°)\\ i_c=I_m\sin(\theta+120°)\end{cases} \tag{34}$$

where I_m is the amplitude of the phase current.

The current flow direction is selected as the positive direction of the current, and the positive direction of the winding flux-linkage and winding current conforms to the right-handed spiral rule. The three-phase voltage balance equation of DMFMCM is as follows.

$$\begin{bmatrix}u_a\\ u_b\\ u_c\end{bmatrix}=\begin{bmatrix}R_a & 0 & 0\\ 0 & R_b & 0\\ 0 & 0 & R_c\end{bmatrix}\begin{bmatrix}i_a\\ i_b\\ i_c\end{bmatrix}+\frac{d}{\mathrm{d}t}\begin{bmatrix}\psi_s\cos\theta\\ \psi_s\cos(\theta-120°)\\ \psi_s\cos(\theta+120°)\end{bmatrix}. \tag{35}$$

The resistance value of each phase is equal, $R_a=R_b=R_c=R_0$.

The electromagnetic torque formula under the electromagnetic equation is as follows.

$$T_e=\frac{1}{2}\left(i_a^2\frac{dL_{aa}}{d\theta}+i_b^2\frac{dL_{bb}}{d\theta}+i_c^2\frac{dL_{cc}}{d\theta}\right)+\left(i_a\frac{d\psi_{ma}}{d\theta}+i_b\frac{d\psi_{mb}}{d\theta}+i_c\frac{d\psi_{mc}}{d\theta}\right). \tag{36}$$

The general formula of the mechanical motion equation of the motor is as follows.

$$T_e=T_m+J\frac{d\omega}{\mathrm{d}t} \tag{37}$$

where Tm is the total load torque of the system, J is the moment of inertia, and ω is the air gap speed.

The load torque is the torque of the entire transmission system, which can be interpreted as the mechanical torque obtained after the torque added to the outer rotor passes through the transmission system. Therefore, equation (36) is the mechanical equation for calculating the electromagnetic torque, which is the dynamics of a structure.

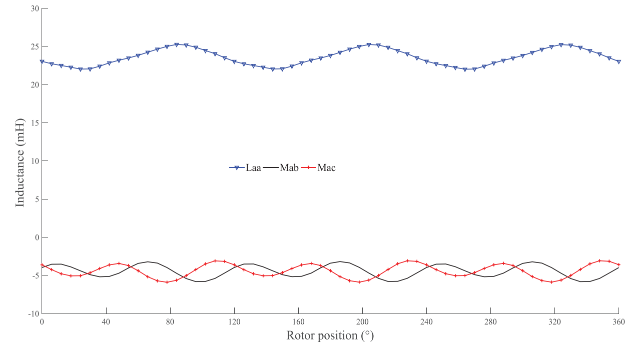

Fig. 10. Phase A inductance calculated by FEA.

According to the mathematical model of DMFMCM in the *abc* coordinate system, the mathematical model in the *d-q* coordinate system can be established, which lays the foundation for the simulation model of DMFMCM and the research of control strategy. In addition, based on the established mathematical model, a simulation model of the DMFMCM motor is built using Simulink simulation software.

3.2 Flux linkage equation in *d-q* coordinate system

The inductance matrix of DMFMCM in the d-q coordinate system is as follows.

$$\begin{bmatrix}L_d & L_{dq} & L_{d0}\\ L_{qd} & L_q & L_{q0}\\ L_{0d} & L_{0q} & L_0\end{bmatrix}=P_{3s/2r}\begin{bmatrix}L_{aa} & M_{ab} & M_{ac}\\ M_{ba} & L_{bb} & M_{bc}\\ M_{ca} & M_{cb} & L_{cc}\end{bmatrix}P_{3s/2r}^{-1} \tag{38}$$

where

$$P_{3s/2r}=\frac{2}{3}\begin{bmatrix}\cos\theta & \cos(\theta-120°) & \cos(\theta+120°)\\ -\sin\theta & -\sin(\theta-120°) & -\sin(\theta+120°)\\ \frac{1}{2} & \frac{1}{2} & \frac{1}{2}\end{bmatrix}$$

L_d, L_{dq}, L_{d0}, L_{qd}, L_q, L_{q0}, L_{0d}, L_{0q} and L_0 are the inductance component in the d-q coordinate system.

Using the FEA method to calculate inductance can be divided into two steps. Firstly, the phase flux linkage ψ_m of the armature winding without current should be calculated; Secondly, the direct current I is applied to one phase of the armature winding, and the total flux linkage ψ of the phase winding is obtained. The total flux linkage is mainly composed of permanent magnet flux linkage and armature flux linkage, which can be expressed as follows.

$$\psi=\psi_m+LI. \tag{39}$$

The phase winding inductance can be calculated as follows.

$$L=\frac{(\psi-\psi_m)}{I}. \tag{40}$$

The calculated inductance is self-inductance when the measured phase and the energized phase are the same phases, and the calculated inductance is mutual inductance when the measured phase and the energized phase are not the same phases. According to the method, the self-inductance and mutual inductance waveforms of phase A are shown in Figure 10.

The phase winding inductance of DMFMCM will periodically change with the change of the rotor position. According to the phase inductance calculated by the FEA method shown in Figure 10, when the rotor d-axis advances the A-phase winding axis θ electrical angle, the three-phase winding inductance can be expressed as follows.

$$\begin{cases} L_{aa} = L_D + L_s\cos(2\theta) \\ L_{bb} = L_D + L_s\cos[2(\theta - 120°)] \\ L_{cc} = L_D + L_s\cos[2(\theta + 120°)] \\ M_{ab} = M_{ac} = M_{ba} = M_{bc} = M_{ca} = M_{cb} = M_D \end{cases} \tag{41}$$

where L_D is the average self-inductance of the phase, L_S is the amplitude of the phase self-inductance fundamental component, and M_D is the average of mutual inductance.

The calculation of inductance component is as follows.

$$\begin{cases} L_d = L_D - M_D - \dfrac{L_s\cos(3\theta)}{2} \\ L_q = L_D - M_D + \dfrac{L_s\cos(3\theta)}{2} \\ L_{dq} = L_{qd} = \dfrac{L_s\sin(3\theta)}{2} \\ L_0 = L_D + 2M_D \end{cases}. \tag{42}$$

According to (41), it can be seen that there is a small cosine component in L_d and L_q. Because DMFMCM adopts a spoke-type inner rotor and a surface-mount outer rotor, it has a "salient pole effect". Furthermore, due to the non-uniform circumferential reluctance caused by the alternating stator slots and the salient pole rotor, a part of the flux linkages on the d-axis and the q-axis turns to each other. Therefore, the mutual inductance L_{dq} between the d and q axes is not 0 but a sine value.

Figure 11 shows the phase self-inductance and mutual inductance of DMFMCM in the abc coordinate system obtained by FEA. The inductance components L_d, L_q, L_0 and L_{dq} calculated by FEA can be obtained according to (37). And the inductance component $L_d{'}$, $L_q{'}$, $L_0{'}$ and $L_{dq}{'}$ in the d-q coordinate system derived by the mathematical model can also be calculated according to (37)–(39). The inductance waveforms calculated by FEA and the mathematical model are shown in Figure 12, and the average inductance is shown in Table 3. As shown in this table, the FEA shows that the average values of L_d and L_q are approximately equal, but the waveforms are different. It can be found that the DMFMCM has a salient pole effect. A comparison of the inductance waveforms in the d-q coordinate system shows that the two waveforms are similar and have small errors, indicating that the inductance results derived from the mathematical model are accurate and valid.

According to the calculation of FEA and mathematical model, the results of the motor inductance in the d-q coordinate system can be obtained as shown in the following Table 3.

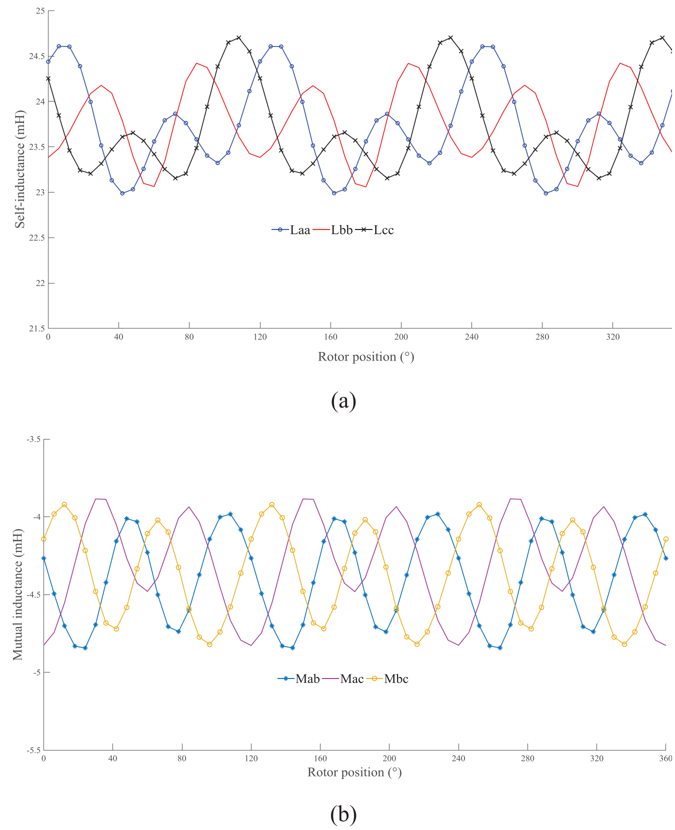

Fig. 11. (a) phase self-inductance and (b) phase mutual inductance in abc coordinate system.

It can be seen from (41) that the inductance components L_d and L_q of DMFMCM on the d-q axis are not constant values, and the mutual inductances L_{dq} and L_{qd} are not zero. Therefore, the flux linkage in the d-q coordinate system can be obtained as follows.

$$\begin{bmatrix} \psi_d \\ \psi_q \\ \psi_0 \end{bmatrix} = \begin{bmatrix} L_q & L_{dq} & L_{d0} \\ L_{qd} & L_q & L_{q0} \\ L_{0d} & L_{0q} & L_0 \end{bmatrix} \begin{bmatrix} i_d \\ i_q \\ i_0 \end{bmatrix} + \begin{bmatrix} \psi_{md} \\ \psi_{mq} \\ \psi_{m0} \end{bmatrix}. \tag{43}$$

Substituting (40) into (42), the flux linkage in the d-q coordinate system can be calculated as follows.

$$\begin{aligned} \psi_d &= \psi_s + L_d i_d + L_{dq} i_q \\ &= \psi_m + \left(L_D - M_D - \frac{L_m\cos(3\theta)}{2}\right) i_d + \left(\frac{L_m\sin(3\theta)}{2}\right) i_q \end{aligned} \tag{44}$$

$$\begin{aligned} \psi_q &= L_q i_q + L_{qd} i_d \\ &= \left(L_D - M_D - \frac{L_{m1}\cos(3\theta)}{2}\right) i_q + \left(\frac{L_m\sin(3\theta)}{2}\right) i_d \end{aligned} \tag{45}$$

where ψ_s is the fundamental wave amplitude of the phase permanent magnet chain under no-load in the abc coordinate system, where ψ_{md}, ψ_{mq}, ψ_0 is calculated as

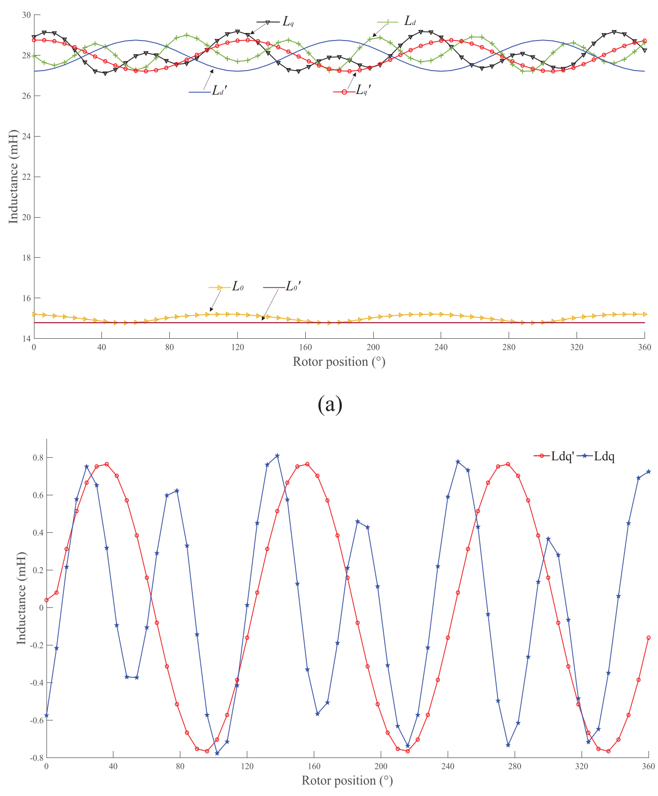

(a)

(b)

Fig. 12. (a) Self-inductance on d-q axis, (b) mutual inductance on d-q axis.

follows.

$$\begin{bmatrix} \psi_{md} \\ \psi_{mq} \\ \psi_{m0} \end{bmatrix} = P_{3s/2r} \begin{bmatrix} \psi_s \cos(\theta) \\ \psi_s \cos(\theta - 120°) \\ \psi_s \cos(\theta + 120°) \end{bmatrix} = \begin{bmatrix} \psi_s \\ 0 \\ 0 \end{bmatrix}. \tag{46}$$

Figure 13 shows the no-load permanent magnet flux waveform of DMFMCM. The values of ψ_{md}, ψ_{mq}, and ψ_{m0} can be calculated, and the flux linkages in the d-q coordinate system can also be calculated by substituting into (43) and (44).

In order to verify the accuracy of the flux linkages of the DMFMCM motor in the d-q coordinate system, the paper adopts the id = 0 control method. The flux linkage waveforms on the d-axis and q-axis are calculated by FEA and mathematical model, as shown in Figure 14. The figure shows that the waveforms calculated by FEA ψ_d and ψ_q are similar to the waveforms obtained by mathematical model $\psi_d{}'$ and $\psi_q{}'$, and the average flux linkage is almost equal. Therefore, it can be found that the flux linkage of DMFMCM calculated by the mathematical model can be verified, and the accuracy of the mathematical model can be ensured.

Table 3. Average inductance in coordinate system.

Parameters	FEA (mH)	Mathematical model (mH)
$L_d(L_d{}')$	28.1009	27.9766
$L_q(L_q{}')$	28.1013	27.9808
$L_0(L_0{}')$	15.0253	14.7751
$L_{dq}(L_{dq}{}')$	–0.016	0

Table 4 shows the average flux linkage of DMFMCM in the d-q coordinate system calculated by the two methods. It can be found that the average flux linkages obtained by the two methods are almost equal to determining the d-axis and q-axis flux linkage components. And through co-simulation, the calculation results of the mathematical model can be verified to ensure the accuracy of the mathematical model.

3.3 Voltage equation in coordinate system

Due to the torque control adopting alternating current, the current in the d-q coordinate system obtained by Park transformation in the abc coordinate system is as follows.

$$\begin{cases} i_d = -I_m \sin(\alpha) \\ i_q = I_m \cos(\alpha) \\ i_0 = 0 \end{cases} \tag{47}$$

where α is the current factor angle, I_m is the current amplitude, and when $\alpha = 0$, it is $i_d = 0$ AC control.

Combining the flux equation and the current equation, the voltage equation of DMFMCM can be calculated.

$$\begin{bmatrix} u_d \\ u_q \\ u_0 \end{bmatrix} = P_{3s/2r} \left(R_0 \begin{bmatrix} i_a \\ i_b \\ i_c \end{bmatrix} + \frac{d}{\mathrm{d}t} \begin{bmatrix} \psi_a \\ \psi_b \\ \psi_c \end{bmatrix} \right) \tag{48}$$

$$\begin{cases} u_d = R_0 i_d + \dfrac{d\psi_d}{\mathrm{d}t} - \omega \psi_q \\ u_q = R_0 i_q + \dfrac{d\psi_q}{\mathrm{d}t} + \omega \psi_d \end{cases} \tag{49}$$

where ω is the rotational angular velocity of the air-gap magnetic field.

3.4 Torque equation in *d*-*q* coordinate system

According to the voltage and current equations in the d-q coordinate system, the electromagnetic torque in the d-q coordinate system can be calculated as follows.

$$\begin{aligned} T_e &= \frac{3p_r}{2}\left(i_q \psi_d - i_d \psi_q\right) \\ &= \frac{3p_r}{2}\left[\psi_m i_q + i_d i_q (L_d - L_q) + L_{dq}\left(i_q^2 - i_d^2\right)\right] \end{aligned}. \tag{50}$$

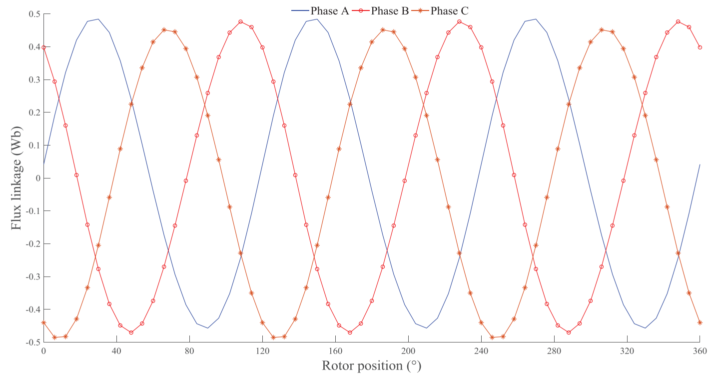

Fig. 13. The no-load flux linkage of DMFMCM.

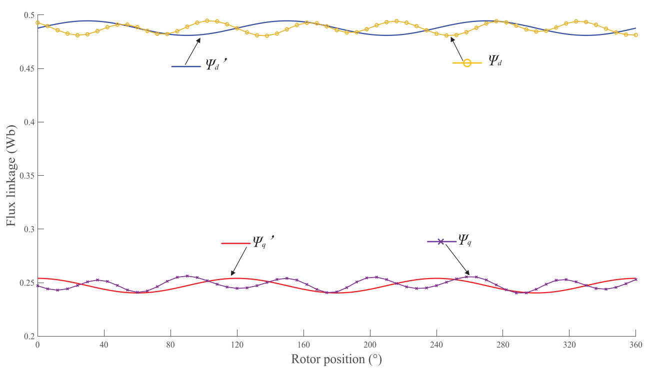

Fig. 14. The flux linkage of DMFMCM on d-q axis.

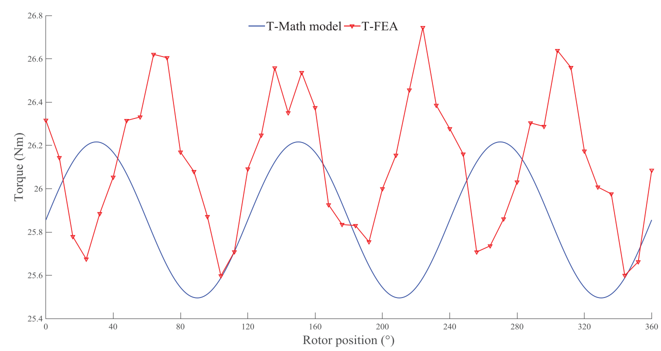

Fig. 15. The torque calculated by FEA and mathematical model.

Table 4. Average flux linkage in d-q coordinate system.

Parameters	FEA (Wb)	Mathematical model (Wb)
$\psi_d(\psi_d{}')$	0.4877	0.4876
$\psi_q(\psi_q{}')$	0.2472	0.2483

Table 5. Electromagnetic torque and torque ripple.

Parameters	FEA (Nm)	Mathematical model (Nm)
$T_e(Nm)$	26.1187	25.8559
$T_{ripple}(\%)$	4.39	2.79

The torque waveform of the DMFMCM obtained after using the mathematical model with $i_d = 0$ and finite element analysis described in this paper is shown in Figure 15. By analyzing and calculating the torque using FEA and mathematical model co-simulation, the torque and torque ripple of DMFMCM can be determined more accurately. As shown in Table 5, the torque waveforms calculated by the two methods are similar, and the torque ripple is also low.

According to the torque obtained in the figure, combined with the (31), the torque ripple calculated by the two methods can be calculated. The calculation results are shown in Table 5.

Based on the mathematical model, the stator winding of the DMFMCM is modelled using Simulink. According to the needs of SVPWM, the whole model adopts a modular design. The stator winding of the DMFMCM requires output current, electromagnetic torque, and rotational angular velocity. Each module is independent and communicated through shared variables. The relationship of the modules can be intuitively seen from the Simulink simulation model of stator windings for DMFMCM and determine the relationship between the parameters. The specific simulation model is shown in Figure 16.

According to the mathematical model, Simulink is used to model the DMFMCM motor. As shown in Figure 16b, three-phase alternating current and total load torque T_m are applied to the motor. After a series of motor coupling actions, three-phase AC I_{abc}, electromagnetic torque T_e and mechanical angular velocity ω_m can be obtained.

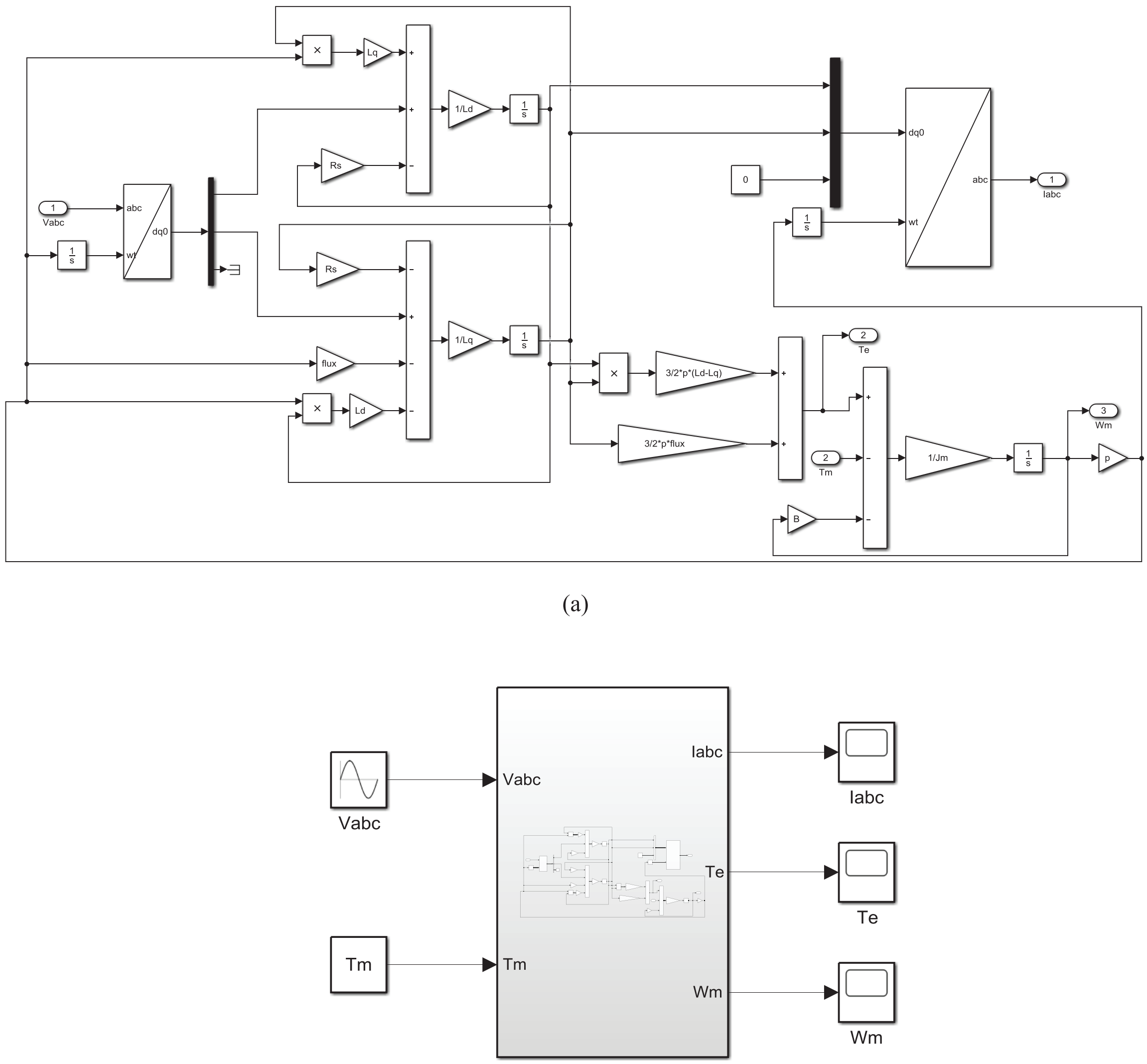

(a)

(b)

Fig. 16. (a) The stator winding model of the DMFMCM simulated by Simulink and (b) the module package of DMFMCM.

4 SVPWM control system

4.1 The principle of SVPWM control system

Space vector pulse width modulation (SVPWM) is a new control strategy for controlling the converter based on the space voltage vector switching of the converter. The core idea of the SVPWM algorithm is to use the inverter space voltage vector switching to obtain a standard circular rotating magnetic field, which enables the AC motor to better control performance by the condition of a low switching frequency. The theoretical basis is the principle of average value equivalence, which combines the voltage vectors within a switching period T_s to make the average value equal to the given voltage vector. According to the working principle of SVPWM, the specific implementation process of the SVPWM algorithm includes three steps: (1) judgment of voltage vector, (2) determination of voltage working time and (3) determination of sector vector switching point.

4.1.1 Judgment of voltage vector

In order to simplify the judgment process, the voltage is equivalently judged. Where $U_\beta = U_{ref}\ \sin\theta$, $U_\alpha = U_{ref} \cos\theta$ Figure 17.

$$\begin{cases} U_a = U_\beta \\ U_b = \dfrac{\sqrt{3}U_\alpha}{2} - \dfrac{U_\beta}{2} \\ U_c = -\dfrac{\sqrt{3}U_\alpha}{2} - \dfrac{U_\beta}{2} \end{cases}. \tag{51}$$

Define intermediate variables A, B, and C, with the following judgments.

- If $U_a > 0$, then $A = 1$, otherwise $A = 0$.
- If $U_b > 0$, then $B = 1$, otherwise $B = 0$.
- If $U_c > 0$, then $C = 1$, otherwise $C = 0$.

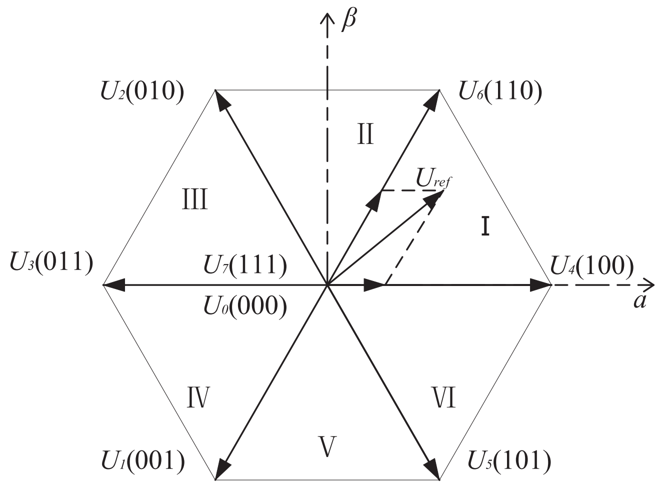

Fig. 17. The relationship between reference vector and space vector.

Table 6. The relationship between N and sector.

N	3	1	5	4	6	2
Sector	1	2	3	4	5	6

Table 7. The relationship between the action time and N.

N	1	2	3	4	5	6
T_1	Z	Y	$-Z$	X	$-X$	$-Y$
T_2	Y	$-X$	X	Z	$-Y$	$-Z$
T_3	$(T\text{-}T_1\text{-}T_2)/2$					

The sector calculation formula is as follows.

$$N = A + 2B + 4C. \tag{52}$$

The sector of the reference voltage vector is determined by N, and the corresponding relationship is shown in Table 6.

4.1.2 Determination of voltage working time

According to the sector where the obtained voltage vector is located, the action time of the space vector can be calculated.

$$\begin{cases} X = \sqrt{3}\dfrac{T}{U_{dc}}U_\beta \\ Y = \dfrac{\sqrt{3}}{2}\dfrac{T}{U_{dc}}U_\beta + \dfrac{3}{2}\dfrac{T}{U_{dc}}U_\alpha \\ Z = \dfrac{\sqrt{3}}{2}\dfrac{T}{U_{dc}}U_\beta - \dfrac{3}{2}\dfrac{T}{U_{dc}}U_\alpha \end{cases}. \tag{53}$$

The U_{dc} is the DC bus voltage, and the assignment relationship corresponding of T_1, T_2, and T_3 is obtained as shown in Table 7.

Table 8. Time switching point of each sector.

N	1	2	3	4	5	6
T_{cm1}	T_B	T_A	T_A	T_C	T_C	T_B
T_{cm2}	T_A	T_C	T_B	T_B	T_A	T_C
T_{cm3}	T_C	T_B	T_C	T_A	T_B	T_A

Saturation judgment is performed on the copied T_1 and T_2. If $T_1+T_2 < T$, then T_1 and T_2 keep unchanged; if $T_1+T_2 > T$, the relationship is as follows.

$$T_1 = \frac{T_1}{T_1+T_2}T \quad T_2 = \frac{T_2}{T_1+T_2}T. \tag{54}$$

4.1.3 Determination of sector vector switching point

According to SVPWM algorithm, it is defined as follows.

$$\begin{cases} T_A = \dfrac{T - T_1 - T_2}{4} \\ T_B = \dfrac{T_1}{2} + T_A \\ T_C = \dfrac{T_2}{2} + T_B \end{cases}. \tag{55}$$

The relationship between the sector vector switching points T_{cm1}, T_{cm2}, T_{cm3} and N can be determined as shown in Table 8.

4.2 Modeling and simulation of SVPWM

According to the results obtained by the SVPWM algorithm, the triangular carrier signal is compared with the vector switching points of each sector to output a PWM pulse signal. The SVPWM is mainly to control the rotor magnetic field. In the rotating d-q coordinate system, the magnetic current and torque current are independently controlled to improve the control performance of DMFMCM. In addition, the mathematical model of DMFMCM in the d-q coordinate system is established. When $i_d=0$, the electromagnetic torque of DMFMCM is only related to the variable i_q, thereby improving the speed regulation performance of the system. The functional block diagram of SVPWM is shown in Figure 18.

As shown in Figure 18, the control strategy includes the current loop, speed loop and SVPWM algorithm, and the SVPWM control of DMFMCM is mainly the control of the current component on the d-q coordinate system. The difference value between the reference speed and the actual speed after power-on is adjusted by the PI regulator, and output is the given value of the q-axis current $i_q{}'$. The three-phase currents i_a, i_b and i_c from DMFMCM are transformed by *Clark* and *Park* to obtain the current components i_d and i_q in the d-q coordinate system. In addition, the given value $i_q{}'$ is compared with the actual value i_q, and then the q-axis voltage $U_q{}'$ adjusted by the PI regulator can be output. In the same

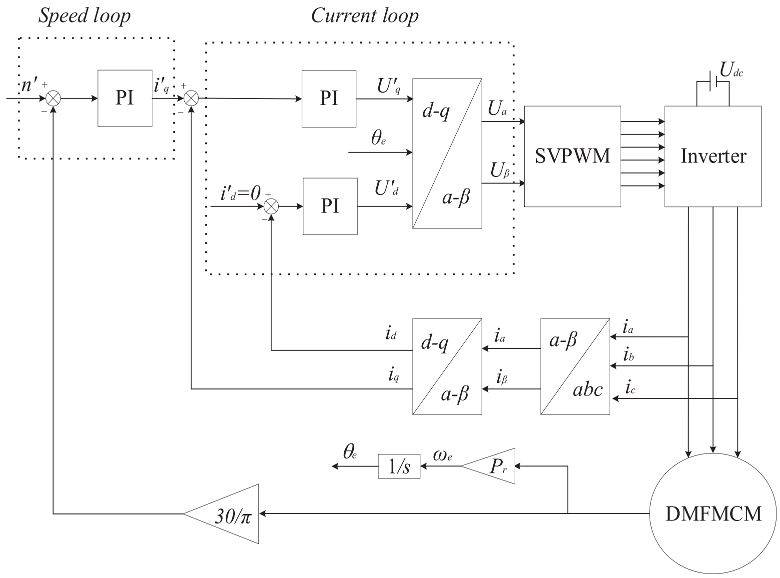

Fig. 18. The functional block diagram of the SVPWM system with $i_d = 0$.

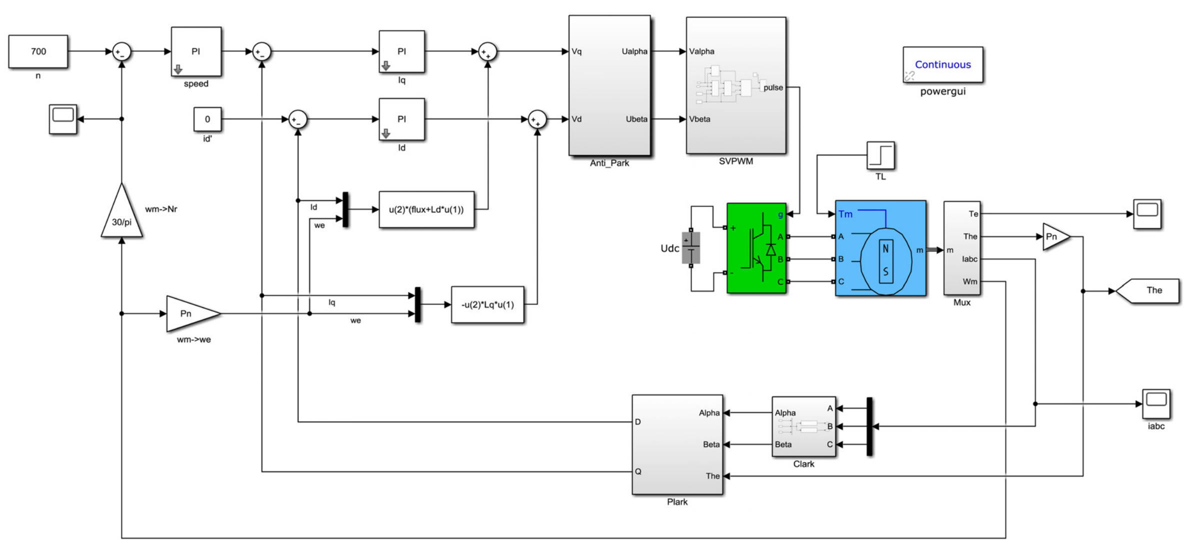

Fig. 19. The SVPWM model of DMFMCM based on $i_d = 0$.

way, the d-axis goes through the same process, and the d-axis voltage $U_d{}'$ is output. $U_q{}'$ and $U_d{}'$ are transformed by *Park* to obtain U_α and U_β, and then the PWM signal is obtained by the SVPWM algorithm to control the inverter. The simulation model of SVPWM established by Simulink is shown in the Figure 19.

The conditions of the simulation model are set as follows: reference speed $n' = 700$ r/min, PWM switching frequency $f = 50$ Hz, simulation time is 0.75 s, variable step size is ode23tb algorithm, relative error is 1e–4. The simulation parameters of DMFMCM are shown in Table 9, the results are shown in Figure 20.

Table 9. Simulation parameters of DMFMCM.

Parameters of DMFMCM	Values
DC bus voltage	$U_{dc} = 311$ V
Stator resistance	$R_s = 2.717\ \Omega$
Flux linkages	$\Psi_m = 0.4877$ Wb
Pole pairs	$p_r = 4$
Moment of inertia	$J = 0.003\,\mathrm{kg/m^2}$
d-axis inductance	$L_d = 28.1009$ mH
d-axis inductance	$L_q = 28.1013$ mH

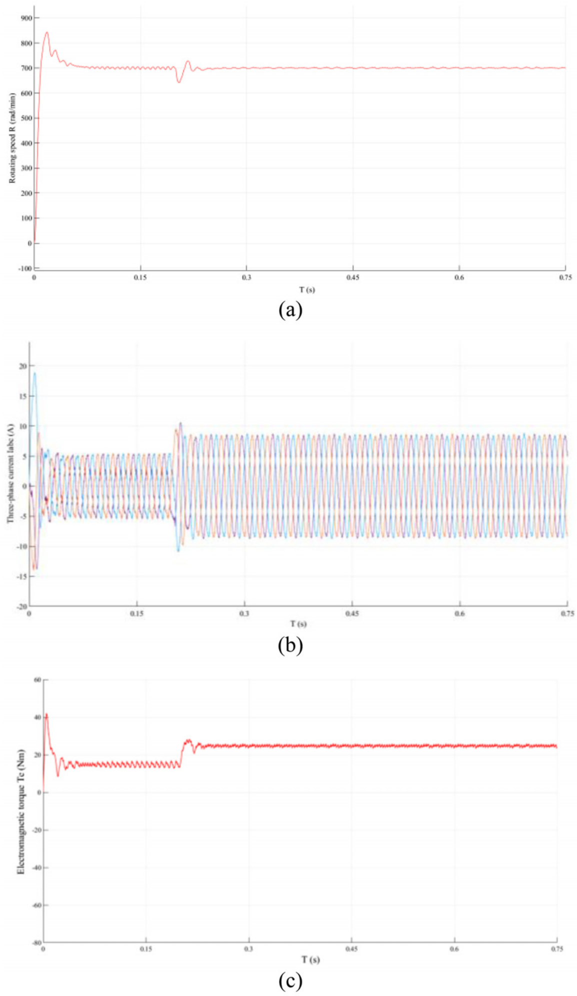

Fig. 20. (a) the simulation curve of motor speed r, (b) the simulation curve of three-phase stator current I_{abc}, and (c) the simulation curve of motor torque T_e.

According to the simulation results shown in Figure 18, the three-phase DMFMCM starts without load. The speed adjusted by the PI regulator will rapidly increase from 0 and exceed the reference speed within 0–0.05 s and will quickly stabilize at the reference speed. At the same time, the torque suddenly increased and stabilized at 16.13 Nm within 0.05 s. At 0.2 s, the rotational speed changes abruptly and immediately stabilize at the reference speed. And the torque also jumped to 25.34 Nm and stabilized. In addition, changes in current are also synchronized with changes in speed and torque. It can be seen that when the electric vehicle starts and shifts, it can output stable torque in a short time, and when shifting and adjusting the speed, the output torque is quickly stable. Therefore, the simulation results show that the SVPWM control is based on PI regulation, which makes DMFMCM have the advantages of start-up and shifting time short, high stability, strong anti-interference ability, and good speed regulation performance.

5 Conclusion

The paper analyzes and studies a new DMFMCM used in electric vehicles. Compared with the conventional magnetic gear compound motor (CMGCM), the DMFMCM has the advantages of strong mechanical strength, high torque density, and low torque ripple. The torque of the outer rotor is 321.02Nm, and the output torque of the outer rotor is 1.4 times that of CMGCM. Furthermore, the torque ripple of the outer rotor is 0.19%, which is only 29.3% of CMGCM. Therefore, the electromagnetic performance of DMFMCM is much better than CMGCM.

The mathematical model of DMFMCM is established, and it is also modelled by Simulink software. The flux linkages equation, electromagnetic torque and voltage equation obtained based on the mathematical model are compared with the FEA simulation results of DMFMCM. According to the FEA and mathematical model co-simulation, the accuracy of the mathematical model is verified through the FEA and mathematical model co-simulation, which lays the foundation for SVPWM control.

This paper establishes a Simulink simulation model of DMFMCM and outputs the results of speed, current and electromagnetic torque based on the input parameters of DMFMCM. It provides a basis for the SVPWM control and verifies the parameters of DMFMCM. By analyzing the principle of SVPWM control, the control strategy mainly includes the speed control loop, current control loop, and SVPWM algorithm. In addition, the system adopts the AC control mode with id = 0, builds a three-phase DMFMCM motor control system model based on PI regulation, and outputs three-phase current, electromagnetic torque and speed. The simulation results show that the SVPWM control strategy makes DMFMCM have the advantages of short start-up shift time, high stability, strong anti-interference ability, and good speed regulation performance, which meets the development needs of electric vehicle drive motors.

Conflict of Interest

The authors declare that they have no known competing financial interests or personal relationships that could have appeared to influence the work reported in this paper.

Financial support

This work was supported by the National Natural Science Foundation of China (Grant No. 51765020), and the Natural Science Foundation of Jiangxi Province (Grant No. 20161BAB206153).

References

[1] E. Ferrero, S. Alessandrini, A. Balanzino, Impact of the electric vehicles on the air pollution from a highway, Appl. Energy **169**, 450–459 (2016)

[2] Z. Li, A. Khajepour, J. Song, A comprehensive review of the key technologies for pure electric vehicles, Energy **182**, 824–839 (2019)
[3] C. Liu, K.T. Chau, C.H.T. Lee, Z. Song, A critical review of advanced electric machines and control strategies for electric vehicles, P. IEEE. PP (99) 1–25 (2020)
[4] S. Madichetty, S. Mishra, M. Basu, New trends in electric motors and selection for electric vehicle propulsion systems, IET Electrical Systems in Transportation (2020).
[5] W. Kong, J. Wang, D. Kong, Y. Cong, S. Feng, Motor shifting and torque distribution control of a multi-motor driving system in electric construction vehicles, Adv. Mech. Eng. **13**, 2072279372 (2021)
[6] Z. Wang, H. Ching, S. Huang, H. Wang, T. Xu, Challenges faced by electric vehicle motors and their solutions, IEEE Access. **9**, 5228–5249 (2021)
[7] C. Huang, F. Lei, X. Han et al., Determination of modeling parameters for a brushless DC motor that satisfies the power performance of an electric vehicle, Measur. Control London Inst. Measur Control. **1**, 52 (2019)
[8] A. Ahmadpour, A. Dejamkhooy, H. Shayeghi, Design and force analysis of salient single-sided linear induction motor, Electr. Power Compound Syst. **49**, 184–198 (2021)
[9] W. Yan, H. Chen, S. Liao, Y. Liu, H. Cheng, Design of a low ripple double modular-stator switched reluctance machine for electric vehicle applications, IEEE Trans. Transport. Electrific. **1**, 99 (2021)
[10] J. Zhao, X. Guan, C. Li, Q. Mou, Z. Chen, Comprehensive evaluation of inter-turn short circuit faults in pmsm used for electric vehicles, IEEE Trans. Intell. Transp. **99**, 1–11 (2020)
[11] K.T. Chau, Z. Dong, J.Z. Jiang, C. Liu, Y. Zhang, Design of a magnetic-geared outer-rotor permanent-magnet brushless motor for electric vehicles, IEEE Trans. Magn. **43**, 2504–2506 (2007)
[12] Y. Fan, L. Zhang, J. Huang, X. Han, Design, Analysis, and sensorless control of a self-decelerating permanent-magnet in-wheel motor, IEEE Trans. Ind. Electr. **61**, 4104–4109 (2014)
[13] G. Cooke, K. Atallah, Pseudo direct drive electrical machines with alternative winding configurations, IEEE Trans. Magn. **53**, 1–8 (2017)
[14] Q. Wang, S. Niu, S. Yang, Design optimization and comparative study of novel magnetic-geared permanent magnet machines, IEEE Trans. Magn. (2017)
[15] H. Zhao, C. Liu, Z. Song, W. Wang, T. Lubin, A dual-modulator magnetic-geared machine for tidal power generation, IEEE Trans. Magn. **99**, 1 (2020)
[16] P. Bellavista, A. Corradi, A. Reale, Quality of service in wide scale publish—subscribe systems, IEEE Commun. Surv. Tutor. **16**, 1591–1616 (2014)
[17] S. Richter, J.A. Quiane-Ruiz, S. Schuh, J. Dittrich, Towards zero-overhead static and adaptive indexing in Hadoop, Vldb J. Int. J. Very Large Data Bases. **23**, 469–494 (2014)
[18] R. Ranjan, Modeling and simulation in performance optimization of big data processing frameworks, IEEE Cloud Comput. **1**, 14–19 (2014)
[19] B. Cao, B.M. Grainger, X. Wang, Y. Zou, Z.H. Mao, Direct torque model predictive control of a five-phase permanent magnet synchronous motor, IEEE Trans. Power Electr. 99 (2020)
[20] Y. Sun, S. Li, X. Fu, W. Dong, B. Balasubramanian, Approximate dynamic programming vector controllers for operation of IPM motors in linear and over-modulation regions, IEEE Trans. Transport. Electrific. **99**, 1 (2020)
[21] Y. Li, M. Jian, J. Liu, Y. Qiang, Voltage vector selection strategy of permanent magnet synchronous motor direct torque control system, in Control Conference (2013)
[22] P.R. Ghosh, A. Das, G. Bhuvaneswari, Performance comparison of different vector control approaches for a synchronous reluctance motor drive, in *International Conference on Computer Applications in Electrical Engineering-Recent Advances* (2017)
[23] T. Li, Q. Yang, B. Peng, Research on permanent magnet linear synchronous motor control system simulation, AASRI Proc. **3**, 262–269 (2012)
[24] X. Wang, L. Ning, R. Na, Simulation of PMSM field-oriented control based on SVPWM, in *IEEE Vehicle Power & Propulsion Conference* (2017)
[25] K. Wang, Z. Gu, Z.Q. Zhu, Z.Z. Wu, Optimum injected harmonics into magnet shape in multiphase surface-mounted pm machine for maximum output torque, IEEE Trans. Ind. Electron. **64**, 4434–4443 (2017)
[26] K. Uppalapati, J. Bird, A flux focusing ferrite magnetic gear, in: 6th IET International Conference on Power Electronics, Machines and Drives (PEMD 2012) (2012)
[27] P. Sarikprueck, P. Lumyong, C.N. Niroiana, C. Attaphong, Magnetization of NdFeB permanent magnet considering demagnetization effect, in *2018 21st International Conference on Electrical Machines and Systems (ICEMS)* (2018)

Cite this article as: J.-G. Wang, B. Zhang, L.-Q. Qian, Research and control of a new dual-modulation magnetic gear compound motor for electric vehicles based on a mathematical model and FEA co-simulation, Mechanics & Industry **24**, 18 (2023)